Spring constant calibration of atomic force microscope cantilevers of arbitrary shape

John E. Sader,[1,2,a)] Julian A. Sanelli,[3] Brian D. Adamson,[3] Jason P. Monty,[4] Xingzhan Wei,[3,5] Simon A. Crawford,[6] James R. Friend,[7,8] Ivan Marusic,[4] Paul Mulvaney,[3,5] and Evan J. Bieske[3]

[1]*Department of Mathematics and Statistics, The University of Melbourne, Victoria 3010, Australia*
[2]*Kavli Nanoscience Institute and Department of Physics, California Institute of Technology, Pasadena, California 91125, USA*
[3]*School of Chemistry, The University of Melbourne, Victoria 3010, Australia*
[4]*Department of Mechanical Engineering, The University of Melbourne, Victoria 3010, Australia*
[5]*Bio21 Institute, The University of Melbourne, Victoria 3010, Australia*
[6]*School of Botany, The University of Melbourne, Victoria 3010, Australia*
[7]*Melbourne Centre for Nanofabrication, Clayton, Victoria 3800, Australia*
[8]*MicroNanophysics Research Laboratory, RMIT University, Melbourne, Victoria 3001, Australia*

(Received 15 June 2012; accepted 18 September 2012; published online 17 October 2012)

The spring constant of an atomic force microscope cantilever is often needed for quantitative measurements. The calibration method of Sader *et al.* [Rev. Sci. Instrum. **70**, 3967 (1999)] for a rectangular cantilever requires measurement of the resonant frequency and quality factor in fluid (typically air), and knowledge of its plan view dimensions. This intrinsically uses the hydrodynamic function for a cantilever of rectangular plan view geometry. Here, we present hydrodynamic functions for a series of irregular and non-rectangular atomic force microscope cantilevers that are commonly used in practice. Cantilever geometries of arrow shape, small aspect ratio rectangular, quasi-rectangular, irregular rectangular, non-ideal trapezoidal cross sections, and V-shape are all studied. This enables the spring constants of all these cantilevers to be accurately and routinely determined through measurement of their resonant frequency and quality factor in fluid (such as air). An approximate formulation of the hydrodynamic function for microcantilevers of arbitrary geometry is also proposed. Implementation of the method and its performance in the presence of uncertainties and non-idealities is discussed, together with conversion factors for the static and dynamic spring constants of these cantilevers. These results are expected to be of particular value to the design and application of micro- and nanomechanical systems in general. © *2012 American Institute of Physics*. [http://dx.doi.org/10.1063/1.4757398]

I. INTRODUCTION

Knowledge of the stiffness of microcantilevers used in the atomic force microscope (AFM) is essential for many applications of the instrument.[1–3] Over the past 20 years, many techniques have been devised for the *in situ* measurement of these spring constants. These methods allow the user to routinely and independently calibrate the spring constants of cantilevers during operation of the AFM. These calibration methods include dimensional approaches,[4–7] methods that probe the static deflection of the cantilever induced by a calibrated load,[8–12] and those that monitor the dynamic vibrational response of the cantilever.[13–18] The performance of these techniques has been widely explored and assessed, and the reader is referred to Refs. 3, 19–22 for detailed reviews.

The method of Sader *et al.*[15] for rectangular cantilevers makes use of the hydrodynamic load experienced by a cantilever as it oscillates in a fluid (such as air) – for clarity, this approach shall henceforth be referred to as the "original method" in this article. It was originally devised for rectangular cantilevers, for which the static normal spring constant k is determined using the formula,[15]

$$k = 0.1906\,\rho\, b^2 L Q\ \Gamma_i(\omega_R)\,\omega_R^2, \tag{1}$$

where ρ is the density of the fluid surrounding the cantilever, b and L are the cantilever width and length, respectively, ω_R and Q are the radial resonant frequency and quality factor in fluid of the fundamental flexural mode, respectively, and $\Gamma_i(\omega_R)$ is the imaginary part of the (dimensionless) hydrodynamic function evaluated at the resonant frequency.[15,23] To implement this formula in practice, knowledge of the fluid density and viscosity, cantilever width and length is required, and the resonant frequency and quality factor must be measured. The technique is independent of the thickness and material properties of the cantilever, which can be difficult to determine in practice. The technique was extended to calibration of the torsional spring constant of rectangular cantilevers in Ref. 24.

Subsequently, the original method was generalized in Ref. 25 to enable measurement of the spring constant of any elastic body, including AFM cantilevers of arbitrary geometry – this shall be referred to as the "general method." The general method relies on knowledge of the hydrodynamic function[28] for a cantilever of arbitrary shape – a protocol for its determination was also presented in Ref. 25. With the (dimensionless) hydrodynamic function for a specific type

a)Author to whom correspondence should be addressed. Electronic mail: jsader@unimelb.edu.au.

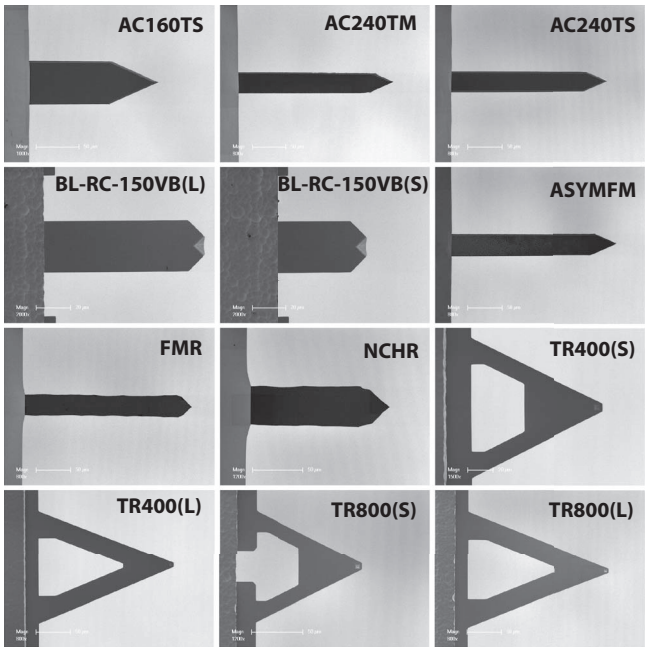

FIG. 1. SEM micrographs showing plan view geometries (shapes) of all cantilevers used in this study. Details of each cantilever, including dimensions, are given in Table I.

of cantilever known (e.g., a particular V-shaped cantilever model), the spring constant of any one of these cantilevers can be determined from knowledge of its plan view dimensions, and measurement of its resonant frequency and quality factor in fluid (typically air). The general method was tested and validated for a series of rectangular and V-shaped cantilevers in Refs. 22 and 25, for which good agreement was found with independent measurements of the spring constants. The theoretical framework underpinning the general method also explained its performance (and that of the original method) under non-ideal but practical conditions, e.g., presence of an imaging tip; see Ref. 25.

Continuous advances in atomic force microscopy have led to the development of a wide array of cantilever designs, as evident from the micrographs presented in Fig. 1. Many of these cantilevers have designs that deviate strongly from a rectangular geometry. Ability to calibrate the spring constants of these cantilevers is thus of critical importance to quantitative AFM measurements. The primary purpose of this article is to report the hydrodynamic functions for a series of cantilevers that are commonly used in the AFM; see Fig. 1. This enables the normal spring constant of these types of cantilevers to be routinely and accurately determined through measurement of their resonant frequency and quality factor in fluid (air). This is regardless of thickness variations, compositional and size changes, provided the plan view geometry (shape) remains constant.[25] As we shall discuss, this prerequisite is commonly satisfied in practice.

The cantilevers studied here possess significant non-idealities in the form of arrow shaped ends, irregular rectangular geometries, small aspect ratio rectangular geometries, non-ideal trapezoidal cross sections of irregular shape and V-shaped geometries. SEM micrographs of these cantilevers are given in Fig. 1. Importantly, the original method[15] implicitly assumes that the cantilever plan view is rectangular and that its aspect ratio (length/width) is large. This is because the fluid-structure theory[23] underpinning this method is derived using this assumption. The method was found to work well for ideally rectangular cantilevers with aspect ratios (length/width) in the range 3.3−13.7, and rectangular cantilevers of non-ideal geometry (ends slightly cleaved with imaging tip) for aspect ratios 3.9–10;[15] the lower limit in aspect ratio for which the original method is valid was not determined in Ref. 15, and left as an open question. Some of the cantilevers shown in Fig. 1 clearly do not satisfy these bounds – they possess smaller aspect ratios, and have irregular and non-rectangular shapes. It is important to emphasize that the general method[25] is valid for any elastic body, and thus it automatically includes all non-ideal effects such as those due to the imaging tip, arbitrary shape, and arbitrary aspect ratio. No corrections to the reported hydrodynamic functions in this article, to account for any such non-idealities, are required or warranted.

The AFM is frequently operated in two complementary modes: (i) "static mode" where the static deflection of the cantilever due to an applied force is monitored, and (ii) "dynamic mode" in which the cantilever is oscillated at or near resonance.[1–3,19–22] Since the deflection functions of the cantilever for these two complementary modes are different, they probe different spring constants. We remind the reader that the spring constant of a cantilever at any point along its length is defined as the second derivative of its potential energy with respect to amplitude at that point.[26] The potential energy can be written in terms of the elastic strain in the cantilever, and therefore depends explicitly on the mode shape, i.e., the deflection function of the cantilever.[27] Consequently, the static and dynamic spring constants of an AFM cantilever will differ, since the deflection functions in these two modes of operation are not identical. These complementary spring constants are needed for quantitative analysis of static and dynamic mode measurements. We therefore present numerical results allowing for conversion between these two spring constants for all cantilevers considered in Fig. 1. This in turn allows the general method to be used to determine both the static and dynamic normal spring constants. The dynamic spring constant for only the fundamental flexural mode is considered in this study.

Experimental protocols for determination of the hydrodynamic function[25,28] and implementation of the original and general methods[22] are summarized. A discussion of the operation of the general method in the presence of random non-idealities, such as uncertainty in cantilever dimensions and cantilever clamping conditions, is also presented.

The article is organized as follows: We begin in Sec. II with a brief exposition of the theory underpinning the general method and the experimental protocol for its implementation. Section III focuses on experimental determination of the hydrodynamic function and implementation of the general method. It is divided into several subsections that provide information on (a) cantilever dimensions, (b) spring constant measurements, (c) measured hydrodynamic functions, (d) a simplified approximate implementation of the general

method valid for any microcantilever, (e) conversion factors for the static and dynamic spring constants, (f) effect of uncertainty on the method, and (g) protocols for implementing the method. Details pertinent to Secs. II and III can be found in the Appendixes.

A. Summary

Readers primarily interested in the hydrodynamic functions for the cantilevers in Fig. 1 are referred directly to Table III and Eq. (10), which are to be used with Eqs. (7a) and (8). This completely specifies the general method for each cantilever. Conversion factors for the static and dynamic spring constants of these cantilevers are given in Table IV.

II. THEORETICAL AND EXPERIMENTAL FRAMEWORK

We first summarize the theoretical framework of the general method, which is applicable to any elastic body or device immersed in a viscous fluid. The device executes resonant oscillations in the fluid. This theoretical framework is then applied to the present case of interest: a cantilever of arbitrary plan view shape undergoing resonant oscillations in its fundamental flexural mode. The experimental protocol for determination of the hydrodynamic function for a cantilever of arbitrary shape is then given. For a detailed derivation of this framework and a comprehensive discussion, the reader is referred to Ref. 25.

A. Arbitrary elastic device in fluid

The principal assumptions of the general method are:

(1) The body behaves as a linearly elastic solid;
(2) Energy dissipation due to vibration of the body occurs in the fluid;
(3) The oscillation amplitude of the body is small, so that all nonlinearities due to the body and fluid are negligible;
(4) The fluid flow generated by the oscillating body is incompressible.

These assumptions are commonly satisfied in practice, from which the maximum energy stored in the oscillating body at resonance directly follows:

$$E_{\text{stored}} = \frac{1}{2} k_d A^2, \tag{2}$$

where k_d is the dynamic spring constant of the oscillation mode, and A is the oscillation amplitude. The energy dissipated in the fluid due to these resonant oscillations can be quantified by the (dimensionless) quality factor,

$$Q \equiv 2\pi \left. \frac{E_{\text{stored}}}{E_{\text{diss}}} \right|_{\omega=\omega_R}, \tag{3}$$

where E_{diss} is the energy dissipated per oscillation cycle, at the resonant frequency ω_R.

Since the flow is linear, as discussed above, the energy dissipated per oscillation cycle will depend on the square of the oscillation amplitude, A. It therefore follows from Eqs. (2) and (3) that the dynamic spring constant (see definition in the Introduction) is related to the quality factor by

$$k_d = \left(\frac{1}{2\pi} \left. \frac{\partial^2 E_{\text{diss}}}{\partial A^2} \right|_{\omega=\omega_R} \right) Q, \tag{4}$$

which is independent of the oscillation amplitude.

In accord with the above-mentioned assumptions, the energy dissipated per cycle E_{diss} must depend on (i) the square of the device oscillation amplitude, A, (ii) the fluid density ρ and shear viscosity μ, (iii) the linear dimension (size) of the device, denoted L_0, (iv) the relevant frequency of oscillation, which from Eq. (4) is the resonant frequency of the device immersed in fluid, ω_R, (v) the mode shape of the vibrating device, and (vi) the geometry of the device. Note that the last two quantities are dimensionless. The relationship between the remaining quantities and E_{diss} can be rigorously determined using dimensional analysis[29] – this gives two dimensionless groups. Use of Buckingham's π theorem[29] then yields the required result for the energy dissipated per cycle,

$$\frac{1}{2\pi} \left. \frac{\partial^2 E_{\text{diss}}}{\partial A^2} \right|_{\omega=\omega_R} = \rho L_0^3 \omega_R^2 \, \Omega(\beta), \tag{5}$$

where $\Omega(\beta)$ is a dimensionless function that depends on the dimensionless parameter,

$$\beta \equiv \frac{\rho L_0^2 \omega_R}{\mu}, \tag{6}$$

which is often termed the inverse Stokes number or Womersley number and is related to the Reynolds number, Re, defined below. Substituting Eqs. (5) and (6) into Eq. (4) gives the required expression for the stiffness, as presented in Ref. 25.

Note that $\Omega(\beta)$ also implicitly depends on the mode shape and geometry of the body, as is evident from the above discussion. Provided these dimensionless quantities do not change, $\Omega(\beta)$ will remain invariant. This point is examined further in Sec. III.

B. Cantilevers of arbitrary shape

The hydrodynamic flow induced by the flexural oscillations of a thin cantilever is dominated by its plan view geometry, with its thickness exerting a negligible effect;[23,30,31] see Sect. II C 1. Since AFM cantilevers typically have both small and large length scales in their plan view geometry, e.g., the width b and length L of the cantilever, these can both affect the flow. We therefore define, without loss of generality,

$$\text{Re} \equiv \frac{\rho b^2 \omega_R}{4\mu} = \left(\frac{b}{2L_0} \right)^2 \beta, \tag{7a}$$

$$\Lambda(\text{Re}) \equiv \frac{L_0^3}{b^2 L} \Omega(\beta). \tag{7b}$$

Note that the linear dimension (size) L_0 is a characteristic length scale of the flow; see Sec. II A. This length scale has been replaced by a combination of the length, L, and width, b, to accommodate details of the flow generated by a vibrating microcantilever. Specifically, the dominant hydrodynamic length scale for the flow is often the smaller length scale, e.g.,

the width b of the cantilever.[23] As such, the flow varies slowly along the cantilever length, L, and rapidly over its width, b.[23] It then follows that the hydrodynamic volume over which energy dissipation occurs scales as b^2L for viscous boundary layers of comparable size to the cantilever width.[23] The rescaling in Eq. (7) thus ensures that the (dimensionless) hydrodynamic function, $\Lambda(\mathrm{Re})$,[28] is an order one quantity in such situations – this case is often encountered in practice,[23] and is demonstrated in Sec. III C. The Reynolds number Re contains the width b only, and can thus be formally interpreted as the squared ratio of the dominant hydrodynamic length scale to the viscous penetration depth. The redefinitions in Eq. (7) thus facilitate physical interpretation and proper normalization of all dimensionless quantities.

Substituting Eq. (7) into Eq. (5) and subsequently into Eq. (4), gives the required formula connecting the dynamic spring constant to the dissipative properties of the cantilever at resonance,

$$k_d = \rho b^2 L\, \Lambda(\mathrm{Re})\, \omega_R^2 Q. \tag{8}$$

Comparing Eq. (8) to Eq. (1) reveals that the general method, which is rigorously applicable to a cantilever of arbitrary shape, yields an equation of identical form to that for a rectangular cantilever. This establishes that the original method, for rectangular cantilevers of high aspect ratio, can be directly extended to cantilevers of arbitrary shape. All that is needed is the hydrodynamic function, $\Lambda(\mathrm{Re})$, for the cantilever geometry and mode in question. Equations (1) and (8) show that the hydrodynamic functions $\Gamma_i(\omega)$ and $\Lambda(\mathrm{Re})$ are related by a constant factor for rectangular cantilevers of high aspect ratio.

Since the static and dynamic spring constants differ by a constant multiplicative factor for a cantilever of fixed plan view geometry, Eq. (8) is equally applicable to the static spring constant under the appropriate renormalization. The renormalization factors for all cantilever geometries in Fig. 1 are given in Sec. III E.

Throughout we only consider the fundamental flexural mode of vibration, even though the general method is rigorously applicable to any mode. Note that the material properties of the cantilever do not enter into the derivation of Eq. (8), and thus the original and general methods are applicable to cantilevers composed of any elastic material. The applicability of these methods to devices whose thickness and/or material properties vary along their length is discussed in Sec. II C.

C. Properties of the general method

In this section, we present a discussion of several features of the general method that are pertinent to its implementation.

1. Effect of finite cantilever thickness

For thin cantilevers executing flexural oscillations, the hydrodynamic function, $\Lambda(\mathrm{Re})$, depends only on the plan view geometry of the cantilever and its mode shape, which are both dimensionless quantities. Cantilever thickness plays a relatively minor role in the hydrodynamic load (and energy dissipation) experienced by a cantilever undergoing flexural oscillations, even for quite thick devices.[30,31] This is because the load is dominated by contributions from the hydrodynamic pressure rather than the shear stress.[30,31] As such, the cantilever plan view dimension to thickness ratio, e.g., the width-to-thickness ratio, does not exert a significant effect on the hydrodynamic function, and can be ignored.[30,31] This property is used in determination of the hydrodynamic function in Sec. II D.

2. Effect of non-uniform cantilever thickness and material properties

Spatial variations in thickness and/or material properties also exert a weak effect on the general method and only enter via their effect on the cantilever mode shape. This is because the right hand side of Eq. (8) depends on the energy dissipated in the fluid, not the cantilever thickness or material; see above. The energy dissipated in the fluid is a weighted average of the mode shape over the cantilever plan view geometry. Since the fundamental mode shape is a simple monotonically increasing function of distance from the clamp, spatial variations in thickness and/or material have a weak effect on this mode shape and hence the general method. This explains recent theoretical findings demonstrating the robustness of the original method, with respect to thickness variations along the cantilever axis, in all but the extreme cases of very strong variations in thickness[32] – in these extreme cases, the mode shape was significantly altered. The same property holds true for the general method.

For the same reason, the presence of an imaging tip mass also has a very minor effect on this mode shape, even in the high tip mass to cantilever mass limit.[25,32] Nonetheless, if the imaging tip is comparable in size to the dominant hydrodynamic length scale of the flow, its presence will enhance the true energy dissipation and thus increase the hydrodynamic function.[24,25] While this can lead to an underestimate of the spring constant obtained using the original method,[25] the general method intrinsically accounts for any such extra energy dissipation. This is because the hydrodynamic function is determined in the presence of the imaging tip; see Sec. II D. As such, the general method is rigorous and accurate in such non-ideal cases.

3. Effect of non-uniform widths and trapezoidal cross sections

Some of the cantilevers in this study possess strongly non-ideal geometries, with varying widths along the cantilever axis and highly scalloped trapezoidal cross sections; see SEM micrographs of the NCHR and FMR devices in Fig. 2. Since the pressure load on the plan view area of a cantilever dominates its hydrodynamic load (see Sec. II C 1 above), and the original and general methods probe the net energy dissipated in the fluid, these geometric properties are inconsequential to the performance of these methods. The maximum width of the trapezoidal cross section should thus be employed in both methods; this explains the finding of Ref. 18. The average of the maximum width is used to

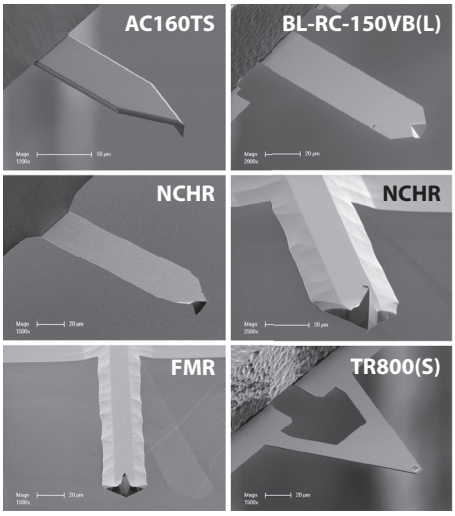

FIG. 2. SEM micrographs showing perspective images for a selection of cantilevers used in this study. All cantilevers used are shown in Fig. 1. Details of each cantilever studied, including dimensions, are given in Table I.

estimate the net energy dissipated by corrugated devices: NCHR and FMR in Fig. 1. The inner width is approximately one third the outer width, see Fig. 2, and is not relevant to the net energy dissipated and hence implementation of the original and general methods.

D. Determination of the hydrodynamic function

We now summarize the experimental protocol[25] to determine the hydrodynamic function, $\Lambda(\mathrm{Re})$, for a cantilever of arbitrary shape – this function is needed to close Eq. (8).

Importantly, the hydrodynamic function is a dimensionless quantity that remains unchanged as the size and/or composition of the cantilever are varied. It is formally the scaled energy dissipation in the fluid and thus depends only on the mode shape and plan view geometry. It is also independent of cantilever thickness for the reasons discussed in Sec. II C. The hydrodynamic function can therefore be determined for all cantilevers of the same plan view geometry by studying a single "test" cantilever immersed in a fluid. Gas is used in these measurements, since it allows for easy modification of its transport properties, produces sharp resonance peaks and thus enables rigorous extraction and measurement of the quality factor.[25]

While theoretical calculations and simulations can be used to determine the hydrodynamic function, performing measurements on a test cantilever (i) automatically accounts for the true geometry of the cantilever device, and (ii) intrinsically includes all complexities such as hydrodynamic coupling between the cantilever and the supporting chip. It also accounts for all non-ideal structures and other effects due to the manufacturing process that may be difficult to quantify and thus theoretically model in an accurate fashion, e.g., shape of imaging tip.[25]

To proceed, we rearrange Eq. (8) to give an expression for the hydrodynamic function in terms of the properties of the cantilever and the gas

$$\Lambda(\mathrm{Re}) = \frac{k_d}{\rho\, b^2 L\, \omega_R^2\, Q}. \tag{9}$$

Our goal is to evaluate the hydrodynamic function over a range of Reynolds numbers, Re, for a single test cantilever. Varying the gas pressure facilitates systematic variation of the Reynolds number, Re, because the gas density and device quality factor are both strongly dependent on gas pressure; the resonant frequency is relatively insensitive to pressure, whereas gas viscosity is invariant. The hydrodynamic function is measured by placing the test cantilever in a pressure chamber, systematically sweeping the gas pressure and recording the gas density, resonant frequency, and quality factor. These results are then substituted into Eqs. (7a) and (9). This can be performed for a number of different gases to ensure consistency between measurements; this is implemented in Sec. III C.

The dynamic spring constant of each test device is also needed to complete the determination of the hydrodynamic function, $\Lambda(\mathrm{Re})$; see Eq. (9). Since the general method requires the hydrodynamic function for its implementation, an alternate calibration method must be employed for this measurement on the test device – the approach used is detailed in Sec. III B and Appendix A.

We emphasize that once the hydrodynamic function, $\Lambda(\mathrm{Re})$, for a particular test cantilever is determined, implementation of the general method for all cantilevers of that same type is independent of the above specified gas pressure and spring constant measurements. This then allows for non-invasive and accurate spring constant measurements of AFM cantilevers in practice using Eq. (8).

III. RESULTS AND DISCUSSION

Hydrodynamic functions for all AFM cantilevers are reported in this section, together with fit functions to facilitate their use in practice. The dimensions and properties of these cantilevers are listed. The apparatus developed for the gas pressure measurements is detailed in Appendix B. Performance of the general method in the presence of non-idealities is also discussed, together with finite element calculations allowing for conversion between the static and dynamic spring constants of all cantilevers. We remind the reader that only the fundamental flexural modes are considered.

A. AFM cantilevers and dimensions

The cantilevers used in this study are from Asylum Research, Nanoworld, and Olympus (Japan); see Fig. 1. These cantilevers are commonly used in practice. They possess significant non-idealities, as outlined above. To highlight their geometric features, perspective SEM images of some of these devices are given in Fig. 2 – other devices possess similar non-idealities to those evident in Fig. 2. No cantilever in this study exhibits an ideal rectangular plan view; such devices were studied previously.[15–20,33,34] Plan view dimensions of all cantilevers were measured from SEM images using ImageJ and a S003 carbon grating replica (2160 lines/mm) as refer-

TABLE I. Measured plan view dimensions (in micrometer) of all cantilevers, as obtained from SEM micrographs. Definitions of the listed dimensions are illustrated in Fig. 3.

Cantilever	b	b_C	d	L	L_C	L_{TIP}
AC160TS	51.0	0	...	151	94.4	151
AC240TM	30.2	0	...	227	196	227
AC240TS	29.6	0	...	229	199	229
BL-RC150VB(L)	29.8	10.1	...	93.1	83.8	93.1
BL-RC150VB(S)	29.9	10.1	...	51.7	42.7	51.7
ASYMFM	31.0[a]	0	...	241	207	241
FMR	30.7 [b]	0	...	242	223	235
NCHR	38.3[c]	0	...	136	107	128
TR400(S)	15.6	...	110	104	...	100
TR400(L)	29.5	...	164	198	...	194
TR800(S)	15.4	...	109	103	...	99.0
TR800(L)	30.4	...	170	206	...	202

[a]Width tapers from clamp to end-tip in the range 32.1–30.6 μm.
[b]Width non-uniform along length, and varies between 28.7 and 32.1 μm.
[c]Width non-uniform along length, and varies between 36.6 and 39.5 μm.
Average width listed in these cases, and used in analysis.

ence; these dimensions are listed in Table I and Fig. 3. The estimated uncertainty in any given dimension measurement is less than 1%.

1. Olympus cantilevers

The devices from Olympus, namely, AC160TS, AC240TM, AC240TS, and the BL-RC150VB, TR400, TR800 series, all have smooth and uniform edges. The arrow-shaped cantilevers (AC160TS, AC240TS, AC240TM) are composed of silicon with reflective aluminum coatings; AC240TM has an additional platinum coating. The imaging tips for AC160TS, AC240TS, and AC240TM are positioned at the very end of the cantilever, i.e., the tip coincides with the maximum extension of the plan view; see Fig. 2. Both biolevers (BL-RC150VB series) are composed of silicon nitride with a reflective gold coating; their imaging tips also coincide with the end of the cantilever and are formed by a depression in the silicon nitride; see Fig. 2. The V-shaped cantilevers (TR400, TR800 series) are also made of silicon nitride with a reflective gold coating. However, their imaging tips are set back from the cantilever end. The TR400 and TR800 cantilevers possess identical plan view geometries, but have thicknesses of 400 and 800 nm, respectively, as specified by the manufacturer. Consequently, they present ideal candidates for demonstrating the invariance of the measured hydrodynamic function to thickness variations between devices.

2. Nanoworld cantilevers

The two Nanoworld devices (FMR, NCHR) exhibit significantly different geometric features to the other quasi-rectangular cantilevers of Asylum Research and Olympus. These cantilevers are composed of silicon with aluminum reflective coatings. However, their widths are non-uniform and vary significantly along their lengths; see Fig. 1. Perspective images of these devices (in Fig. 2) reveal that they possess

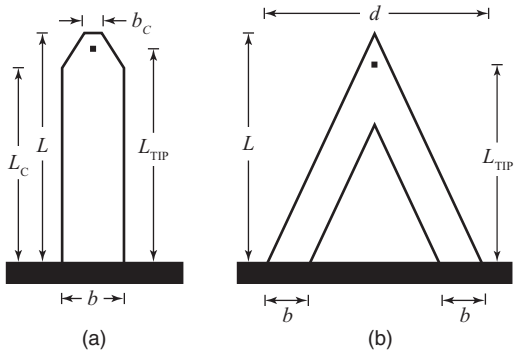

FIG. 3. Schematic diagrams of all cantilevers in Fig. 1, illustrating dimensions listed in Table I. (a) Quasi-rectangular cantilevers; (b) V-shaped cantilevers. Position of imaging tip shown as a square dot.

quasi-trapezoidal cross sections with pronounced scalloping of their sloped edges along the cantilever length. Their imaging tips are set back from the cantilever end. Given their non-uniform geometries, these devices allow the robustness of the original and general methods to be assessed in the presence of significant non-idealities.

3. Asylum Research cantilever

The cantilever from Asylum Research, ASYMFM, is of identical geometry to the Olympus AC240TS and AC240TM devices. It is also composed of silicon but has a CoCr magnetic coating. The imaging tip coincides with the end of the cantilever. It possesses a slightly tapered plan view with its width slightly narrowing from the clamp to the cantilever end; see Table I.

B. Spring constants of test cantilevers

The dynamic spring constant of each test cantilevers was measured noninvasively by monitoring its Brownian motion under ambient conditions using a laser Doppler vibrometer (LDV). This approach eliminates additional uncertainties inherent in the standard AFM thermal method[3,14,16,19,20] that arise from calibration of the AFM photodiode displacement sensitivity. These uncertainties originate from a number of factors and include required corrections for laser position and finite spot size, non-ideal contact and friction between the cantilever tip and sample, compliance of the sample, and conversion factors relating the cantilever angle-to-displacement under static and dynamic loads;[16,20,35,36] these vary with the cantilever used. Since the spring constant is inversely proportional to the displacement squared in this method, the additional uncertainty introduced by these effects is doubled in all AFM thermal method measurements. Elimination of these additional uncertainties is thus highly desirable in the present study and is achieved by using a LDV; see Appendix A for details. Instruments calibrated to the SI standard (e.g., see Ref. 37) provide an alternate approach for measuring the spring constants of the test cantilevers; these were not implemented in this study.

We emphasize that these LDV measurements are needed only for the test cantilevers to determine their hydrodynamic functions. The general method is specified independently of

TABLE II. Measured dynamic spring constants k_d of the test cantilevers, at their imaging tip positions, using a laser Doppler vibrometer (uncertainty based on a 95% confidence interval). Resonant frequencies f_R and quality factors Q in air (1 atm) also shown.

Cantilever	k_d (N/m)	f_R (kHz)	Q
AC160TS	57.3 ± 1.9	370	646
AC240TM	1.65 ± 0.065	65.9	162
AC240TS	2.90 ± 0.13	83.0	213
BL-RC150VB(L)	0.00683 ± 0.00017	12.4	12.5
ASYMFM	2.13 ± 0.055	69.4	187
FMR	2.19 ± 0.085	70.6	163
NCHR	33.9 ± 1.5	299	480
TR400(S)	0.0971 ± 0.0052	34.6	39.7
TR400(L)	0.0293 ± 0.0027	11.8	21.5
TR800(L)	0.194 ± 0.0062	22.9	57.1

the LDV instrument once these measurements have been performed. The determined hydrodynamic functions then allow for accurate noninvasive calibration of these cantilever types using the general method, Eq. (8), regardless of their plan view dimensions, composition, and thickness variations; see Secs. I and II.

Several measurement points along the cantilever were interrogated to ensure robust measurements. Details of these measurements are given in Appendix A. The measured dynamic spring constants at the imaging tip position of each cantilever are listed in Table II; uncertainties due to fitting the spring constant data at all measurement points are listed in Table II and discussed in Appendix A. These are typically between $\pm 2\%$ and $\pm 5\%$ based on a 95% confidence interval. Since the LDV does not possess additional significant uncertainties in velocity, due to its inherent calibration relative to the speed of light, these observed fit uncertainties specify the total uncertainties in the measured spring constants; see Appendix A. The measured resonant frequency and quality factor in air (1 atm) for each cantilever are also given, and possess smaller uncertainty: between $\pm 0.0006\%$ and $\pm 0.02\%$ for the resonant frequency, and $\pm 0.3\%$ and $\pm 1\%$ for the quality factor.[53] The spring constants of two test cantilevers, BL-RC150VB(S) and TR400(L), could not be measured; also see Appendix A.

C. Hydrodynamic functions

The hydrodynamic function for each test cantilever was determined by measuring its resonant frequency and quality factor as a function of gas pressure; see Sec. II D. These results were then combined with the measured plan view dimensions and spring constant (Secs. III A and III B), and substituted into Eqs. (7a) and (9) to give the required hydrodynamic function. The experimental procedure and apparatus developed for the gas pressure measurements are detailed in Appendix B.

To ensure accurate data collection, independent measurements were performed using two different gases: dry nitrogen (N_2) and carbon dioxide (CO_2). One reason for using CO_2 is that it possesses a kinematic viscosity (shear viscosity/density) a factor of two lower than that of air, at 1 atm.[54] This in turn yields a Reynolds number, Re, a factor of two higher than the result in air; see Eq. (7a). Any subsequent measurement on another cantilever in air, with a resonant frequency twice that of the test cantilevers, will thus be within the characterized range of Re. Importantly, the use of CO_2 eliminates the need to use gas pressures larger than 1 atm to increase the upper limit of Re.[25]

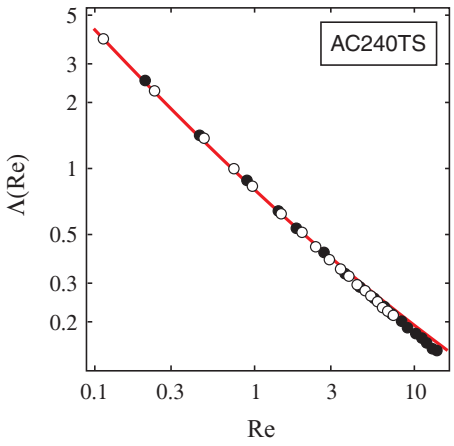

FIG. 4. Measured hydrodynamic function of the AC240TS device using N_2 (open circles) and CO_2 (filled circles). Theoretical result (solid line) calculated using Eq. (20) of Ref. 23.

1. Quasi-rectangular cantilevers

We first assess the robustness of the characterization protocol underpinning the general method. This is illustrated for cantilevers with quasi-rectangular plan views. The hydrodynamic function of the AC240TS device is given in Fig. 4. Independent measurements in N_2 and CO_2 overlap precisely, illustrating the accuracy of the measurements – we remind the reader that the kinematic viscosities of these gases differ by a factor of two. Also shown is the theoretical result for the hydrodynamic function, as calculated using Eq. (20) of Ref. 23. Note the excellent agreement between all three data sets – there are no adjustable parameters in this comparison. Since the theoretical result for the hydrodynamic function is used implicitly in the original method (for rectangular cantilevers), the level of agreement in Fig. 4 demonstrates the validity of the original method for this type of device. The original method and the general method coincide in this case because their hydrodynamic functions overlap.

Figure 5 compares the measured hydrodynamic functions for the AC240TS, AC240TM, ASYMFM, and FMR devices, which have similar plan view geometries. Note that (i) these devices have different stiffnesses, resonant frequencies, and quality factors, see Table II, and (ii) measurements on each device were performed in both N_2 and CO_2. The measured hydrodynamic functions for all these devices again overlap with each other and with the theoretical prediction of Ref. 23, see Fig. 5. The FMR device possesses a scalloped trapezoidal cross section, in contrast to the uniform cross sections of the other devices; see Fig. 2. The average of the maximum width of such cantilevers should be used in the

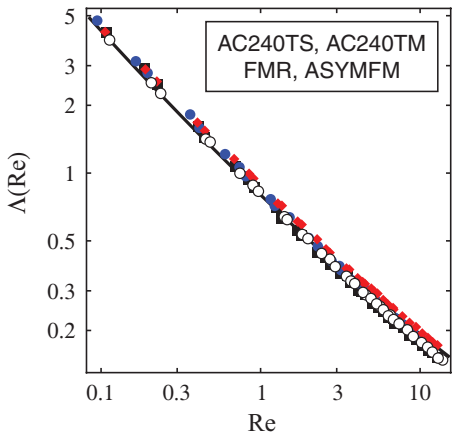

FIG. 5. Measured hydrodynamic function of the AC240TS (open circles), AC240TM (filled circles), ASYMFM (squares) and FMR (diamonds) devices using both N_2 and CO_2. Theoretical result (solid line) calculated using Eq. (20) of Ref. 23.

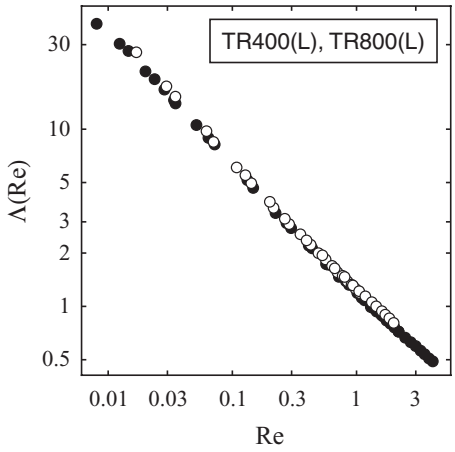

FIG. 6. Measured hydrodynamic functions of the TR400(L) (open circles) and TR800(L) (filled circles) devices using both N_2 and CO_2. These devices have identical plan view geometries but their thicknesses differ by a nominal factor of two.

original and general method; see Sec. II C 3. As discussed in Sec. II C, this non-uniformity in cross section is inconsequential to both methods – the measured hydrodynamic functions for all devices overlap over the entire Reynolds number range studied. This establishes that the original and general methods coincide for all these devices and demonstrates the robustness of these methods.

2. Non-rectangular cantilevers

Next, we demonstrate the validity of the general method for non-rectangular geometries by comparing the measured hydrodynamic functions for the TR400(L) and TR800(L) devices. These cantilevers possess identical plan view geometries, but differ in thickness by a nominal factor of two. Their measured resonant frequencies also differ by a factor of approximately two (11.8 and 22.9 kHz) while their dynamic stiffnesses are vastly different, in agreement with theoretical considerations; see Table II. Since the hydrodynamic function is only sensitive to the plan view geometry, and this is identical for these two devices, the independently measured hydrodynamic functions for these two devices are expected to coincide. This is borne out in Fig. 6, where overlap of the (independent) measurements on these two different devices is observed. This fundamental property is used in Sec. III C 3 to derive a single fit function for the hydrodynamic function of devices with identical plan view geometries.

The AC160TS and BL-RC150BV(L) cantilevers also have strongly non-ideal geometries. The AC160TS device does not satisfy the fundamental requirement for use of the original method: a rectangular plan view of large aspect ratio (length/width); it has an arrow shaped geometry. While the BL-RC150BV(L) device has a rectangular geometry, its aspect ratio is small (length/width ∼3), with a significant imaging tip. The performance of the original and general methods for these cantilevers, in comparison to higher aspect ratio quasi-rectangular cantilevers, is discussed in Sec. 3 of Appendix A. Overlap in the measured hydrodynamic functions using N_2 and CO_2, as observed in Figs. 4–6, was also found for the AC160TS and BL-RC150BV(L) devices (data not shown).

The results in Figs. 4–6 and measurements for the AC160TS and BL-RC150BV(L) devices, serve to demonstrate the robustness of the experimental protocol and validity of the general method for both quasi-rectangular and non-rectangular plan view geometries of varying composition.

3. Formulas for hydrodynamic functions

To facilitate their use in practice, analytical formulas for all hydrodynamic functions were obtained by fitting the measured data to the following functional form:

$$\Lambda(\mathrm{Re}) = a_0 \mathrm{Re}^{a_1 + a_2 \log_{10} \mathrm{Re}}, \tag{10}$$

where a_0, a_1, and a_2 are constant coefficients, specific to each type of cantilever. This functional form was chosen because the hydrodynamic function is approximately linear on a log-log scale and is a monotonically decreasing function of Re; see Figs. 4–6. Fitting the data to a second-order polynomial on a log-log scale yields the general form in Eq. (10). The resulting fit coefficients a_0, a_1, and a_2 for all test devices are presented in Table III.

Three sets of devices have identical plan view geometries: (1) AC240TS, AC240TM, ASYMFM; (2) TR400(L),

TABLE III. Coefficients a_0, a_1, and a_2 in functional form Eq. (10) for measured hydrodynamic functions $\Lambda(\mathrm{Re})$ of test cantilevers.

Cantilever	a_0	a_1	a_2
AC160TS	0.7779	−0.7230	0.0251
AC240TM, AC240TS, ASYMFM	0.8170	−0.7055	0.0423
BL-RC150BV(L)	1.0025	−0.7649	0.0361
BL-RC150BV(S)	...	−0.7613	0.0374
FMR	0.8758	−0.6834	0.0357
NCHR	0.9369	−0.7053	0.0438
TR400(S), TR800(S)	1.5346	−0.6793	0.0265
TR400(L), TR800(L)	1.2017	−0.6718	0.0383

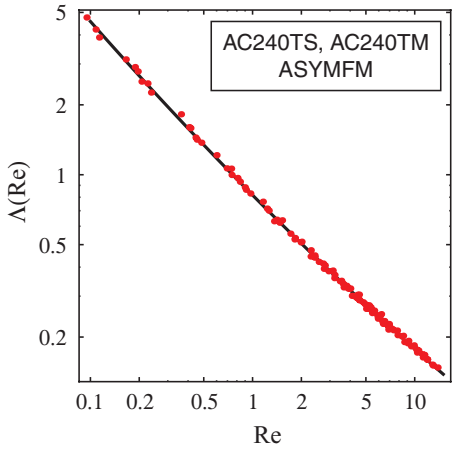

FIG. 7. Combined data of measured hydrodynamic functions for AC240TS, AC240TM, and ASYMFM devices (red dots), and resulting fit of this data to Eq. (10) (solid line). Fit coefficients are given in Table III. These devices have identical plan view geometries.

TR800(L); (3) TR400(S), TR800(S). The hydrodynamic functions within each set must therefore coincide. Single fit functions for each set were determined in the following manner. Set (1): The fit function was evaluated by combining independent data from all cantilevers in this set, and fitting the result to Eq. (10). The combined data and fit function for Set (1) is given in Fig. 7; similar fits were obtained for other sets and devices (not shown). Set (2): Since the measured spring constant of TR400(L) possesses greater uncertainty than TR800(L) [see Table II and Appendix A], its measured spring constant was not used but chosen such that its hydrodynamic function overlapped precisely with that of the TR800(L) device over the entire Reynolds number regime. This yielded a spring constant 5% lower than that reported in Table II, which is within its measured uncertainty. These combined data were then fit to Eq. (10). Set (3): The spring constant of the TR800(S) device could not be measured; see Appendix A. Rather than discarding this data, its spring constant was chosen such that the hydrodynamic function for the TR800(S) coincided with that of the TR400(S) device over the entire Reynolds number range studied – again excellent overlap was observed. The resulting data were fit to Eq. (10). While single devices could have been used to determine the hydrodynamic function for each of these sets, the chosen redundancy of devices facilitates accurate evaluation of the hydrodynamic functions.

a. Evaluation of unknown coefficients Note that the coefficient a_0 for the BL-RC150VB(S) test device is not specified, because its spring constant could not be measured and no other device studied possesses an identical geometry. Nonetheless, the results in Table III can in the future be used to generate the hydrodynamic function, $\Lambda(\mathrm{Re})$, for this device model by performing independent measurements on other test cantilevers, of identical geometry. The dimensions and materials need not be the same, but the plan view geometry (shape) must remain unchanged. All that is required is knowledge of the plan view dimensions of the additional device, measurement of its resonant frequency and quality factor in gas (at a single known pressure) and its stiffness. From these measurements, the Reynolds number, Re, of the additional device follows and the value of the hydrodynamic function at this Reynolds number is immediately determined using Eq. (9). This value can then be substituted into the fit formula for $\Lambda(\mathrm{Re})$, in Eq. (10) and Table III, from which the coefficient a_0 is uniquely specified. Using this procedure, the hydrodynamic function $\Lambda(\mathrm{Re})$ for the BL-RC150VB(S) device can be evaluated.

b. Refinement of hydrodynamic functions The procedure outlined immediately above allows the accuracy of the presented hydrodynamic functions to be enhanced. This for example could involve calibrating additional test cantilevers using methodologies referenced to the SI standard.[37] These additional measurements would lead to a refinement in the coefficient a_0.

c. Uncertainty analysis All fit functions specified in Table III possess uncertainties of less than $\pm 1\%$ (based on a 95% confidence interval), relative to measured data for the hydrodynamic function. Note that the data are well represented by a simple power-law as specified by a_0, a_1 (see above discussion regarding linearity on a log-log scale) – the higher-order correction due to a_2 exerts a minor influence. Measurements of the dynamic spring constants introduce additional uncertainty of approximately $\pm 2\%$ to $\pm 5\%$ (also based on a 95% confidence interval) into the coefficient a_0 only; the coefficients a_1 and a_2 are unaffected by the spring constant. It is noteworthy that individual fits to the hydrodynamic functions for devices with identical plan views differ by only a few percent, e.g., individual fits to data for AC240TM, AC240TS, and ASYMFM. This is in line with the measured spring constant uncertainty and the use of an empirical fit function to represent the measured data; see above. Combining the data from devices with identical plan view geometries yields a more accurate estimate of the hydrodynamic function, and is reported in Table III.

d. Scaling behavior The scaling chosen in Eq. (7) was motivated by the expectation that the dominant hydrodynamic length scale is given by the minimum plan view dimension of the cantilever. This is strongly supported by the values of a_0 in Table III, which are all of order unity, i.e., the hydrodynamic functions $\Lambda(\mathrm{Re})$ are of order unity when the Reynolds number is one, as required; see discussion in Sec. II B.

Note that the hydrodynamic functions for the V-shaped cantilevers, TR400 and TR800, are larger in magnitude to those for other devices. This is expected because V-shaped cantilevers possess two skewed rectangular arms, enhancing the net hydrodynamic load and hence energy dissipation.

It is interesting that the hydrodynamic functions of all devices exhibit a power-law dependence on Reynolds number of approximately $\mathrm{Re}^{-0.7}$, i.e., $a_1 \sim -0.7$; see Table III. This can be understood by considering the following asymptotic limits. In the high Reynolds number limit ($\mathrm{Re} \gg 1$), the hydrodynamic function is expected to scale as $\mathrm{Re}^{-1/2}$ due to

the presence of thin viscous boundary layers in the vicinity of the cantilever surface. In the opposite (creeping flow) limit of low Reynolds number ($\mathrm{Re} \ll 1$), a scaling behavior of Re^{-1} must be exhibited. Thus, the observation in measurements of a power-law dependence intermediate to these two limiting cases is not unexpected, since the Reynolds number is of order unity for all devices studied. This property can be used to devise an approximate method that circumvents the need for pressure measurements. This is discussed in Sec. III D.

D. Simplified approximate implementation of the general method

The general method relies on knowledge of the hydrodynamic function, $\Lambda(\mathrm{Re})$, which can be measured for a single "test" device using the gas pressure protocol discussed in Sec. II D; these measurements are reported in Sec. III C. Importantly, the preceding discussion demonstrates that the hydrodynamic function of a microscale device (whose Reynolds number is of order unity) is well approximated by

$$\Lambda(\mathrm{Re}) \approx a\mathrm{Re}^{-0.7}, \tag{11}$$

where the coefficient a depends only on the plan view geometry of the device model in question.

Since only one coefficient is unknown in Eq. (11), a single measurement on a test device is required to determine its value. For example, by measuring the spring constant, resonant frequency, and quality factor of a test device in air, the value of a then directly follows from Eqs. (7a), (9), and (11):

$$a = \left.\frac{k_d \mathrm{Re}^{0.7}}{\rho\, b^2 L\, \omega_R^2\, Q}\right|_{\text{test device}}, \tag{12}$$

where all parameters on the right hand side of Eq. (12) are determined from this single test measurement.

Equations (11) and (12) then uniquely specify the hydrodynamic function for arbitrary Reynolds numbers. While this approach introduces a systematic error into the general method (since Eq. (11) is approximate), this error is expected to be small since the power-law dependence of the hydrodynamic function is bounded between -0.5 and -1; see Sec. III C. This error is of course minimized if the Reynolds number of the test device is comparable to (other) devices of the same geometry to be calibrated.

If the test cantilever has identical plan view dimensions to any subsequent (uncalibrated) device, Eqs. (9) and (12) simplify, yielding

$$k_d = k_{d,\text{test}} \frac{Q}{Q_{\text{test}}} \left(\frac{f_R}{f_{R,\text{test}}}\right)^{2-\alpha}, \tag{13}$$

where $\alpha = 0.7$ (see above), the subscript "test" refers to the (known) test cantilever parameters, and all other parameters are for the uncalibrated device. Equation (13) thus enables the spring constant k_d for an uncalibrated device to be easily determined from measurement of its resonant frequency and quality factor alone. The actual dimensions of the test and uncalibrated devices are not required; they simply need to be identical. Note that small deviations in the plan view dimensions between the test and uncalibrated devices have a minimal effect, for reasons discussed in Sec. III F.

TABLE IV. Conversion factors relating the dynamic k_d and static k_s spring constants of all devices in this study. These are evaluated at the imaging tip positions; see Table I. Finite element (FE) analysis is used for all calculations based on geometries as measured from SEM micrographs. The FE mesh is systematically refined to ensure convergence of 99.9%. Poisson's ratio of 0.25 is used in all calculations.

Cantilever	k_d/k_s
AC160TS	1.101
AC240TM, AC240TS, ASYMFM	1.043
BL-RC150VB(L)	1.035
BL-RC150VB(S)	1.042
FMR	1.029
NCHR	1.036
TR400(S), TR800(S)	1.054
TR400(L), TR800(L)	1.072

The above approximate implementation of the general method facilitates the calibration of microscale devices in situations where equipment for the required pressure measurements is not available.

E. Conversion factors for static and dynamic spring constants

As discussed in Sec. I, either the static or dynamic spring constant is needed for quantitative measurements, depending on the mode of operation. Importantly, the general method can be applied to measure both the static and dynamic spring constants. In results for the hydrodynamic function presented in Sec. III C, the dynamic spring constant of the fundamental flexural mode was used. To calibrate the static spring constant associated with a static force applied at the imaging tip position, conversion factors between these two spring constants are required. These were calculated using finite element analysis,[38] and are given in Table IV. Devices with identical plan view geometries gave identical results to within dimensional uncertainty; the average of these results is reported. Note that the conversion factors in Table IV are dimensionless and thus independent of the cantilever dimensions.

F. Effect of dimensional uncertainty on the general method

Next, we study the effect of uncertainty in the plan view dimensions on the spring constant determined by the general method. Naive inspection of Eq. (8) appears to suggest that the resulting uncertainty in the spring constant scales with the cube of the plan view dimensions. However, the width of the cantilever, b, is embedded in the hydrodynamic function via the Reynolds number; see Eq. (7a). Since the hydrodynamic function scales as Re^{a_1}, to leading order, it follows that the spring constant scales as $b^{2(1+a_1)}L$ in the general method; note that $a_1 \sim -0.7$ as discussed above. As such, the measured spring constant exhibits a weak dependence on the cantilever width with sub-linear scaling; the dependence on cantilever length is linear. This leads to an overall uncertainty in the measured spring constant that scales with the $\sim 3/2$ power of the plan view dimensions. Consequently, knowing the plan

view dimensions only approximately, imposes a weak penalty on the overall uncertainty of the method.

Measurement of the hydrodynamic function $\Lambda(\mathrm{Re})$, for a single test cantilever, also exhibits this robustness to dimensional uncertainty. The uncertainty in the measured hydrodynamic function again scales with the $\sim 3/2$ power of the test device plan view dimensions. This is evident by comparing Eqs. (7a) and (9), which are used in the measurement of $\Lambda(\mathrm{Re})$, to the power-law dependence, Re^{a_1}, of the hydrodynamic function.

The general method has been implemented so that the dynamic spring constant is determined at the imaging tip position of all test cantilevers. If the cantilever under consideration has a different tip position, relative to the cantilever length, the spring constant will need to be adjusted; the imaging tip positions of the test cantilevers are specified in Table I. This adjustment can be achieved using the following properties: (i) the normal spring constant varies approximately with the cube of the distance along the cantilever length,[39–41] and (ii) this spring constant is insensitive to tip position variations parallel to the clamp.[39]

G. Implementation of the original and general methods

We now summarize some practical issues relevant to implementation of the original and general methods:

(1) Measurement of the thermal noise spectrum facilitates determination of the resonant frequency and quality factor, by eliminating any spurious effects due to the frequency response of the piezoactuator.[42,43] Thus, while active excitation of the cantilever can be used to measure these fundamental quantities, and may be desirable for very stiff cantilevers,[15] interrogation of the thermal noise poses fewer issues and is simple to implement.

(2) Hydrodynamic functions for the original and general methods were determined for cantilevers well away from any surface, i.e., gas surrounding the cantilever was assumed to be unbounded. This implicit assumption must therefore be satisfied in all implementations of these methods, since proximity to a surface can reduce the measured quality factor due to squeeze film damping – this would lead to an (artificial) underestimate of the spring constant. Since the dominant hydrodynamic length scale for many cantilevers is given by their width, the thermal noise spectra of cantilevers should be measured at least several widths away from any solid surface. Exploration of these effects and measurement protocols for implementation of the original and general methods have been reported in Refs. 22, 44, and 45.

(3) The resonance behavior of a cantilever is independent of the measurement position along its axis, provided a measurement is not taken at a zero of the slope of its deflection function (for which no signal may result). This is always satisfied for the fundamental flexural mode of a cantilever, away from the clamp. Consequently, the original and general methods are insensitive to position of the measurement laser on the cantilever plan view and the laser spot size. These quantities are not required and can be specified arbitrarily provided the signal-to-noise is sufficient.

(4) The original and general methods yield the spring constants directly and do not require knowledge of the absolute deflection of the cantilever. Consequently, the equipartition theorem can be used to calibrate the displacement sensitivity of the optical lever deflection system commonly used in the AFM, from the measured spring constant. This approach was proposed and systematically studied in Ref. 46 for a series of rectangular cantilevers – the same method is applicable to non-rectangular cantilevers.[22]

(5) Some cantilevers possess a significant "over-hang" at the clamped end, due to the manufacturing process, e.g., see TR400(S) and TR800(S) devices in Fig. 1. Since the general method only requires the mode shape of the vibrating structure to be identical to the test cantilever, such non-idealities do not pose an issue. The displacement near the base of the cantilever is always small, and hence its contribution to the net energy dissipation is small. The general method is therefore expected to be robust to such non-ideal variations.

(6) An "under-hang" would shorten the overall length of the vibrating structure and could affect the net hydrodynamic load and energy dissipation. To understand its effect, consider a long rectangular cantilever of high aspect ratio (length/width). The presence of an under-hang would reduce the overall length of the cantilever, while not changing its geometry. Since the original method scales linearly with the cantilever length, this would have a weak effect for under-hangs of relatively small length in comparison to the cantilever length, if the original length were used; use of the shortened length would eliminate this effect. For non-rectangular cantilevers, their geometry may also be affected in addition to a change in cantilever length. Nonetheless, this effect is still expected to be weak unless the under-hang were a significant fraction of the cantilever length.

(7) The original and general methods are most easily implemented in air, at 1 atm. The density and viscosity of air are thus required. These are weakly dependent on atmospheric variations in temperature and pressure, and are insensitive to humidity. Even so, for more precise measurements the temperature and pressure should be measured and SI data used to determine the true density and viscosity.

IV. CONCLUSIONS

Ability to characterize the static and dynamic mechanical properties of AFM cantilevers and in general, micro- and nanomechanical devices, is critical to many applications. Manufacturing and measurement specifications often lead to device geometries that are complex and non-ideal. Dynamic methods provide a versatile tool for extracting the mechanical properties of such devices. In this study, previous work on ideal rectangular cantilevers has been extended and applied to actual devices currently employed. Specifically, we have

presented hydrodynamic functions for a series of non-ideal and non-rectangular cantilevers that are commonly used in practice. These functions allow the spring constants of these cantilevers to be easily and routinely determined from measurements of the resonant frequency and quality factor in fluid (such as air). Performance of the original method[15] in the presence of non-idealities was also examined. For all quasi-rectangular cantilevers of high aspect ratio (length/width), the original and general methods agreed closely. This demonstrated the robustness of both methods to the presence of non-idealities. For highly non-rectangular cantilevers, robustness of the experimental protocol and general method was also confirmed and deviations between the original and general methods were discussed. Simple and accurate formulas for the hydrodynamic functions of all cantilevers were presented to facilitate implementation in practice. A simplified approximate implementation of the general method was proposed, facilitating implementation of the general method when the specified gas pressure measurements are not available. Finally, conversion factors relating the dynamic and static spring constants of all cantilevers studied were presented, together with a discussion of practicalities for implementing the original and general methods.

ACKNOWLEDGMENTS

The authors would like to thank the Melbourne Centre for Nanofabrication for access to the MSA-400 Micro System Analyzer, and Toby Ban, Jerome Eichenberger, and Mario Pineda from Polytec Headquarters, Irvine, CA, for use of the MSA-500 Micro System Analyzer. This research was supported by the Australian Research Council Grants Scheme. An iPhone application implementing the general method for the cantilevers used in this study is available from: http://www.ampc.ms.unimelb.edu.au/afm/.

APPENDIX A: SPRING CONSTANT MEASUREMENTS

The dynamic spring constants of the fundamental flexural modes of all test cantilevers were measured using a LDV;[47–49] MSA-400 and MSA-500 Micro System Analyzers, Polytec (Waldbronn, Germany). The LDV provides an independently calibrated measurement of velocity using a laser system that incorporates a modified Mach-Zehnder interferometer.[50] The spot size of the incident LDV laser is nominally 1 μm, allowing for precise placement and subsequent measurement of cantilever velocity at any position on its plan view – all cantilever plan view dimensions are an order of magnitude larger than the optical spot size.

The spring constants were determined by monitoring the Brownian fluctuations of each cantilever. The equipartition theorem provides a unique connection between the mean squared velocity of the device, $\langle v^2 \rangle$, and its dynamic spring constant, k_d, at the measurement position[48]

$$k_d = \omega_R^2 \frac{k_B T}{\langle v^2 \rangle}, \tag{A1}$$

where k_B is Boltzmann's constant and T is absolute temperature. Note that k_d and $\langle v^2 \rangle$ in Eq. (A1) are specified at the same measurement position on the cantilever.

1. Spring constant at the imaging tip position

LDV measurement sensitivity is intrinsically dependent upon strong reflection of the incident laser – sensitivity is degraded on highly curved surfaces. Curved or slanted surfaces are thus not easily interrogated, and direct measurement at the tip position was therefore not always possible. Spring constants at the tip positions were always determined by measuring the dynamic spring constant at a series of defined positions along the cantilever length – absolute distance calibration of these points was not required. Interpolation between these data point values and extrapolation allowed for the dynamic spring constant at the tip position to be acquired. This was achieved by fitting the measured spring constants to the function

$$k_d = k_d^{\text{tip}} (1 - \alpha\, x)^{-\beta}, \tag{A2}$$

where k_d^{tip} is the required spring constant at the imaging tip position, k_d is the spring constant at the LDV measurement position, x is the (uncalibrated) measurement position along the cantilever relative to the imaging tip position, and α and β are constants. Choice of this functional form is driven by the corresponding result for the static spring constant, for which $\beta = 3$.[39,40,51] The dynamic spring constant possesses a slightly weaker dependence on position, which motivates the use of an adjustable constant power-law, β.

To demonstrate the validity of this approach, a comparison is made to calculations from Euler-Bernoulli theory for a beam with a uniform cross section along its major axis; see Fig. 8. Note that the data point closest to the cantilever end is a significant distance away (10% of the cantilever length). An absolute length scale along the cantilever axis is not required and is automatically determined by fitting the data to Eq. (A1)

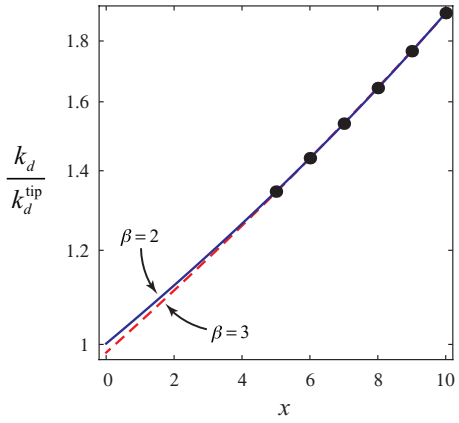

FIG. 8. Theoretical simulation of fitting procedure, Eq. (A2), to extract the dynamic spring constant at the imaging tip position. Solid circles are data calculated using Euler-Bernoulli beam theory. Lines are fits to this data using Eq. (A2). Each unit on the horizontal axis is 0.02 L, where L is cantilever length; point furthest back from end-tip is at a distance of 0.2 L. Imaging tip coincides with the end-tip here. (Upper fit curve [blue]) $\beta = 2$; (Lower fit curve [red]) $\beta = 3$.

using k_d^{tip} and α as adjustable parameters; fixed values of β were used in Fig. 8.

The resulting fits are excellent and yield spring constants at the cantilever end that are within 1% of the required value. The choice of β is not important and varying this value in the range $2 \leq \beta \leq 3$ results in only a ~1% variation in the extrapolated end-tip spring constant – the fit constant α accommodates any change in β; see Fig. 8. The choice of data point positions along the cantilever axis also has a minimal effect. This demonstrates the robustness of the fitting procedure, which enables the spring constant at the imaging tip position to be determined from independent measurements away from this position.

2. LDV measurements

Time series measurements of the Brownian fluctuations (velocity) of the cantilever were taken at 5 specified points along the cantilever axis, and processed to determine the thermal noise spectra at each point.[52] These velocity power spectra were then fitted to the response of a harmonic oscillator, incorporating a white noise floor, A_{white}, to yield the resonant frequency, f_R, quality factor, Q, and velocity power spectral density (PSD) at resonance, B,

$$S(f) = A_{\text{white}} + \frac{B\, f_R^4}{Q^2\left(f^2 - f_R^2\right)^2 + f^2 f_R^2}. \tag{A3}$$

Using these measured fit parameters, the mean squared velocity immediately follows:

$$\langle v^2 \rangle = \frac{\pi\, B\, f_R}{2\, Q}, \tag{A4}$$

which is substituted into Eq. (A1) to obtain the required dynamic spring constant. Note that Eqs. (A3) and (A4) implicitly assume that the power spectra are single-sided and all frequencies are in Hertz; these are related to the radial frequencies by $\omega = 2\,\pi f$.

To ensure thermal drift did not affect measurements, and to accommodate software limitations, time series of short duration (~20–30 s) were measured at each spatial position along the cantilever. Measurements were performed in a temperature-stabilized environment (clean room), which reduced such effects. Minimizing thermal drift is critical because the dynamic spring constant depends strongly on position, and movement of the laser on the cantilever will affect measurements.

These measurements were performed by first placing a virtual grid on the cantilever; see Fig. 9(a). Each point on the grid was manually selected, the laser system refocused and the time series subsequently acquired. Two independent measurements using the protocol in Sec. 1 were performed on each device, and the overall mean and standard error computed; 5 measurement points along the device were used in each independent measurement. A sample of the measured thermal noise spectra, measurement grid, dynamic spring constants and fits to Eqs. (A2) and (A3) are given in Fig. 9 for the AC160TS device.

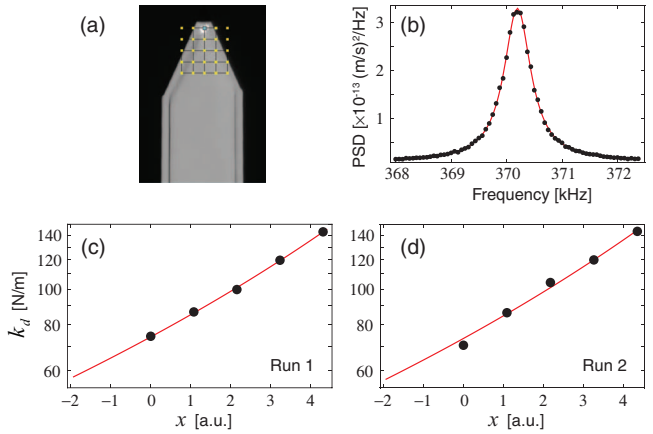

FIG. 9. LDV measurement of dynamic spring constants for AC160TS device, showing (a) LDV measurement grid, (b) thermal noise spectrum, (c) dynamic spring constants at grid positions (Run 1), and (d) dynamic spring constants at grid positions (Run 2). Fits of Eq. (A2) to LDV data in (c) and (d) also shown (solid lines). Any drift in grid positions at each measurement point was measured and included in the analysis in (c) and (d).

Dynamic spring constants of the test cantilevers in Fig. 1 at their imaging tip position, as measured using the above protocol, are given in Table II. These spring constants were observed to exhibit uncertainties in the vicinity of ±2 to ±5% based on a 95% confidence interval of the fitted data, which are also reported in Table II. Deviations in linearity of LDV velocity measurements are estimated at ±0.1%, and uncertainties due to the fit procedure of Sec. 1 are less than ±1%. The listed uncertainties in Table II thus represent the total uncertainties in the measured spring constants. We did not calibrate LDV measurements to a SI standard, with reported uncertainties being due to scatter in fits to the spring constant data only; see Sec. III C 3. The observed uncertainties are explored below.

Note that the spring constants for two cantilevers, BL-RC150VB(S) and TR800(S), could not be measured due to coincidence of the fundamental mode resonance peak and an unrelated instrumentation peak originating from the LDV. These instrumentation peaks occur at 32.8 and 65.5 kHz and are known to be due to the A/D encoders in the LDV; these coincide with 2^{15} and 2^{16} Hz, respectively.

Uncertainty in the mean squared velocity, as obtained by fitting Eq. (A3) to the measured PSD, is given by[53]

$$\frac{\text{SD}\,[\langle v^2 \rangle]}{\langle v^2 \rangle} = \sqrt{\frac{3\, Q}{2\pi\, f_R \tau}}, \tag{A5}$$

where τ is the total measurement time and SD is the standard deviation. Equation (A5) predicts a standard deviation of less than 1% for the spring constant at each measurement point along the AC160TS device, cf. Eqs. (A1) and (A5). This underestimates the uncertainty in Fig. 9 where larger scatter at individual measurement points is observed. Nonetheless, the fitted spring constant is determined very accurately and exhibits an overall uncertainty of ±3% based on a 95% confidence interval (±2 standard errors). Comparing repeat measurements on the same cantilever, cf. Figs. 9(c) and 9(d), highlights this feature.

The TR400(L) device exhibited significantly larger uncertainty (±9%) in its measured spring constant in comparison to all other devices; see Table II. This was peculiar to the TR400(L) device and may be related to the optical nature of its surface. Importantly, overall spring constant uncertainty in the TR800(L) device is low (±3%), and good agreement is found between the hydrodynamic functions for the TR400(L) and TR800(L) devices; see Fig. 6. Since the TR400(L) and TR800(L) devices have identical plan view geometries, the anomalous uncertainty in the spring constant for the TR400(L) device is inconsequential to practical implementation of the general method – they present redundant (and identical) measurements of the hydrodynamic function for this plan view geometry; see Sec. III C 3.

These findings indicate that spring constant measurements using the LDV instrument are very accurate (uncertainties of approximately ±2% to ±5%) when sufficient care is taken. Measurement of the spring constant at a single position on the cantilever is prone to error, and should be avoided. Protocols such as that specified above, which make use of multiple positions, are desirable for accurate and robust measurements.

3. Small aspect ratio cantilevers

The cantilevers, BL-RC150VB(L) and AC160TS, exhibit small aspect ratios (length/width ∼3), highly non-ideal plan view geometries, cleaved ends, and imaging tips. These devices violate a fundamental tenet of the original method: a cantilever of rectangular plan view with a large aspect ratio.

End effects can be pronounced for such small aspect ratios. The AC160TS device possesses a severely cleaved end, which strongly reduces the net hydrodynamic load in comparison to a complete rectangle – its plan view geometry is non-rectangular. This gives rise to a significant overestimate (68%) in the spring constant using the original method. The end-tip of the BL-RC150VB(L) device is less cleaved, but contains a depressed and relatively large imaging tip. The original method underestimates the LDV measurement of the spring constant by 19%. This suggests that the presence of the imaging tip is dominating that of the cleaved end to enhance the net hydrodynamic load, as described in Ref. 25.

Devices of higher aspect ratio circumvent these effects. For example, the AC240TS and AC240TM devices possess similar cleaved ends to the AC160TS device but have much larger aspect ratios – the original method works well for these high aspect ratio devices; see Figs 4 and 5.

Importantly, the general method is insensitive to these considerations and handles cantilevers of any geometry, material, and non-ideality.

APPENDIX B: GAS PRESSURE DEPENDENT MEASUREMENTS

1. Apparatus and procedure

Each cantilever was mounted in a small, aluminum gas cell equipped with an o-ring sealed glass window; see Fig. 10. The optical beam from a laser (HeNe, Thorlabs

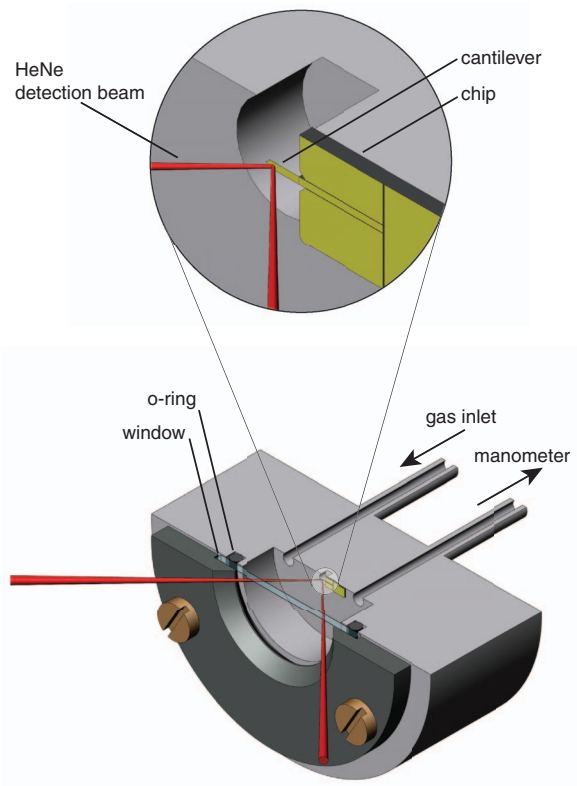

FIG. 10. Apparatus for measurement of thermal noise spectra of individual cantilever devices as a function of gas pressure.

633 nm, 1.5 mW) was focused by a 60 mm focal length lens onto the back of the cantilever end-tip. The reflected beam was detected using a quadrant photodiode (OSI Optoelectronics) acting as a bi-cell detector. The photodetector signal was amplified (EG&G Princeton Applied Research 5113), band pass filtered to remove noise at frequencies away from the cantilever resonance, and sent to a data acquisition board (Data Translation DT9832-04-2-BNC, 16-bit) to enable further processing in software. A sampling frequency of 200 kHz was used for the low frequency cantilevers ($f_R < 100$ kHz) and 900 kHz for the high frequency cantilevers. Noise was attenuated by a band pass filter with 6 dB/octave low frequency and high frequency roll-offs typically at less than 0.75 f_R and greater than 1.25 f_R, respectively.

Gas was delivered through an inlet tube at the rear of the cell and its absolute pressure measured with a capacitance manometer (MKS Baratron, 0–1000 Torr) connected directly to the cell; see Fig. 10. Pressure inside the cell was adjusted using a gas inlet and vacuum line system. Gas from a regulated bottle supply was admitted through a needle valve, allowing for the precise adjustment of pressure. The vacuum side of the line was regulated using a valve that led to the vacuum pump (Edwards E2M2 Two Stage Rotary Vane, 46 L/min). Changing from one gas to another involved shutting the gas supply at the regulator, evacuating the line and cell for at least 20 min before back-filling with the new gas and then pumping down to the desired starting pressure. Generally, the series of measurements was made in order of increasing pressure, although measurement series taken with decreasing pressure showed that the order had no bearing on

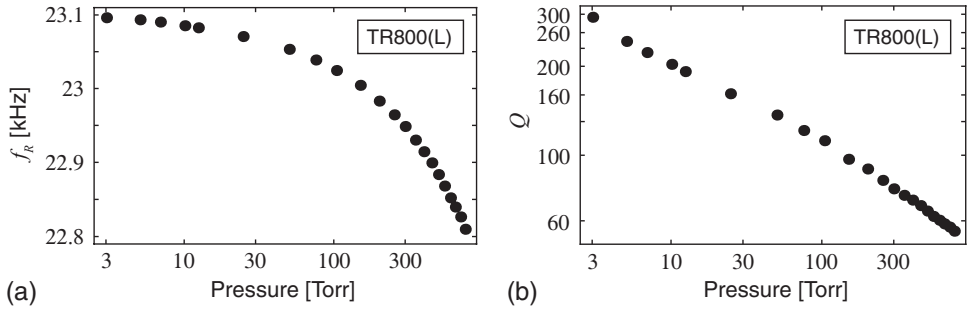

FIG. 11. Measurements of (a) resonant frequency, and (b) quality factor as a function of gas pressure for the TR800(L) device, using CO_2.

the results. The chamber pressure tended to drift slightly during the 2 min data acquisition period, so the mean pressure over this duration was used for the calculations. In all cases, this drift was less than 2% of the mean, and most measurements were made with a pressure drift much less than 1%.

The ambient temperature in the laboratory also varied slightly (1–2 °C). To account for this effect the cell temperature was measured at the start and finish of each pressure-series run using a thermocouple, and the mean temperature recorded. The pressure and mean temperature were then used to determine the gas density and viscosity from SI standard data.[54]

Cantilever data were recorded at a series of pressures, which encompassed the continuum and transition flow regimes. Only the former is relevant to the present analysis, but measurements over the entire range were taken for completeness.[25] All cantilevers were measured at 18 different pressures ranging from 10 to 760 Torr, with some devices probed at 4 additional pressures in the range 1–10 Torr. Use of many measurement pressures enabled robust fitting of the analyzed gas pressure data and hence accurate determination of the hydrodynamic functions; see Sec. III C.

The time series signal at each pressure was fast Fourier transformed using MATLAB software. The acquisition duration was 120 s for each pressure. The resulting time series was subdivided into sections each with 2^{16} points, which were Fourier transformed and averaged together to yield the required power spectral density. To account for spectral distortion due to finite frequency resolution, the true quality factor was determined from measurements using Eq. (B1).

2. Determination of the true quality factor

Finite frequency resolution in the power spectral density reduces the measured quality factor Q from its true value; see Ref. 55. Use of a rectangular window enables the true device quality factor to be extracted from this measured value

$$Q_{\text{true}} = \frac{\pi f_R}{2\delta f}\left(1 - \sqrt{1 - Q_{\text{meas}}\frac{4\delta f}{\pi f_R}}\right), \qquad \text{(B1)}$$

where Q_{true} is the (required) true quality factor of the device, f_R and Q_{meas} are the (fitted) measured resonant frequency and quality factor using Eq. (A3), respectively, and δf is the frequency division in the thermal noise spectrum. Use of Eq. (B1) eliminates systematic offset due to this artifact, which can be ∼10%, depending on the frequency resolution. Equation (B1) was used in measurements of the quality factor, which are required for determination of the hydrodynamic function. However, Eq. (B1) was not used to determine the cantilever spring constants via the equipartition theorem, Eq. (A4). This is because the area under the resonance peak is unaffected by finite frequency resolution (even though the quality factor is reduced);[55] the power spectral density at resonance decreases in synchrony with the quality factor.

3. Sample measurements

A sample of the gas pressure measurements is given in Fig. 11. Both the resonant frequency and quality factor increase monotonically as gas pressure is reduced, in line with previous observations.[25,39,56–58] The quality factor displays a strong dependence on gas pressure, whereas the resonant frequency is relatively insensitive. The measurements span two orders of magnitude in pressure. This allows the Reynolds number, Re, to be determined over a similar range because gas density is proportional to pressure; see Sec. II D. Similar qualitative trends to those apparent in Fig. 11 were observed for all test cantilevers. Scatter in measurements of the resonant frequency and quality factor, as obtained from fits to the PSD of Brownian motion, was due to sampling noise inherent in periodogram estimates of the PSD.[53]

[1]R. Garcia and R. Perez, Surf. Sci. Rep. **47**, 197 (2002).
[2]F. J. Giessibl, Rev. Mod. Phys. **75**, 949 (2003).
[3]H.-J. Butt, B. Cappella, and M. Kappl, Surf. Sci. Rep. **59**, 1 (2005).
[4]J. E. Sader and L. White, J. Appl. Phys. **74**, 1 (1993).
[5]J. M. Neumeister and W. A. Ducker, Rev. Sci. Instrum. **65**, 2527 (1994).
[6]C. A. Clifford and M. P. Seah, Nanotechnology **16**, 1666 (2005).
[7]J. Lubbe, L. Doering, and M. Reichling, Meas. Sci. Technol. **23**, 045401 (2012).
[8]H.-J. Butt, P. Siedle, K. Seifert, K. Fendler, T. Seeger, E. Bamberg, A. L. Weisenhorn, K. Goldie, and A. Engel, J. Microsc. **169**, 75 (1993).
[9]T. J. Senden and W. A. Ducker, Langmuir **10**, 1003 (1994).
[10]C. T. Gibson, G. S. Watson, and S. Myhra, Nanotechnology **7**, 259 (1996).
[11]M. Tortonese and M. Kirk, Proc. SPIE **3009**, 53 (1997).
[12]A. Torii, M. Sasaki, K. Hane, and S. Okuma, Meas. Sci. Technol. **7**, 179 (1996).
[13]J. P. Cleveland, S. Manne, D. Bocek, and P. K. Hansma, Rev. Sci. Instrum. **64**, 403 (1993).
[14]J. L. Hutter and J. Bechhoefer, Rev. Sci. Instrum. **64**, 1868 (1993).
[15]J. E. Sader, J. W. M. Chon, and P. Mulvaney, Rev. Sci. Instrum. **70**, 3967 (1999).
[16]H.-J. Butt and M. Jaschke, Nanotechnology **6**, 1 (1995).
[17]R. Levy and M. Maaloum, Nanotechnology **13**, 33 (2002).
[18]A. D. Slattery, J. S. Quinton, and C. Gibson, Nanotechnology **23**, 285704 (2012).

[19]J. E. Sader, in *Encyclopedia of Surface and Colloid Science*, edited by A. Hubbard (Dekker, New York, 2002), pp. 846–856.
[20]S. M. Cook, T. E. Schäffer, K. M. Lang, K. M. Chynoweth, M. Wigton, R. W. Simmonds, and K. M. Lang, Nanotechnology **17**, 2135 (2006).
[21]M. L. B. Palacio and B. Bhushan, Crit. Rev. Solid State Mater. Sci. **35**, 73 (2010).
[22]J. te Riet, A. J. Katan, C. Rankl, S. W. Stahl, A. M. van Buul, I. Y. Phang, A. Gomez-Casado, P. Schön, J. W. Gerritsen, A. Cambi, A. E. Rowan, G. J. Vancso, P. Jonkheijm, J. Huskens, T. H. Oosterkamp, H. Gaub, P. Hinterdorfer, C. G. Figdor, and S. Speller, Ultramicroscopy **111**, 1659 (2011).
[23]J. E. Sader, J. Appl. Phys. **84**, 64 (1998).
[24]C. P. Green, H. Lioe, J. P. Cleveland, R. Proksch, P. Mulvaney, and J. E. Sader, Rev. Sci. Instrum. **75**, 1988 (2004).
[25]J. E. Sader, J. Pacifico, C. P. Green, and P. Mulvaney, J. Appl. Phys. **97**, 124903 (2005).
[26]H. Goldstein, C. Poole, and J. Safko, *Classical Mechanics* (Addison-Wesley, San Francisco, 2002).
[27]S. Timoshenko and J. N. Goodier, *Theory of Elasticity* (McGraw-Hill, New York, 1969).
[28]Λ(Re) is strictly the imaginary component of the hydrodynamic function, as defined in Ref. 23. It is referred to as the hydrodynamic function in this article for simplicity.
[29]P. W. Bridgman, *Dimensional Analysis* (Yale University Press, New Haven, 1931).
[30]D. R. Brumley, M. Willcox, and J. E. Sader, Phys. Fluids **22**, 052001 (2010).
[31]R. Cox, F. Josse, S. M. Neinrich, O. Brand, and I. Dufour, J. Appl. Phys. **111**, 014907 (2012).
[32]H. Frentrup and M. S. Allen, Nanotechnology **22**, 295703 (2011).
[33]T. Pettersson, N. Nordgren, M. W. Rutland, and A. Feiler, Rev. Sci. Instrum. **78**, 093702 (2007).
[34]J. W. M. Chon, P. Mulvaney, and J. E. Sader, J. Appl. Phys. **87**, 3978 (2000).
[35]R. Proksch, T. E. Schaeffer, J. P. Cleveland, R. C. Callahan, and M. B. Viani, Nanotechnology **15**, 1344 (2004).
[36]J. Stiernstedt, M. W. Rutland, and P. Attard, Rev. Sci. Instrum. **76**, 083710 (2005).
[37]K.-H. Chung, S. Scholz, G. A. Shaw, J. A. Kramar, and J. R. Pratt, Rev. Sci. Instrum. **79**, 095105 (2008).
[38]COMSOL Multiphysics, Gottingen, Germany.
[39]J. E. Sader, I. Larson, P. Mulvaney, and L. R. White, Rev. Sci. Instrum. **66**, 3789 (1995).
[40]J. E. Sader, Rev. Sci. Instrum. **66**, 4583 (1995).
[41]R. J. Roark and W. C. Young, *Formulas for Stress and Strain*, 5th ed. (McGraw-Hill, New York, 1975).
[42]T. E. Schaeffer, J. P. Cleveland, F. Ohnesorge, D. A. Walters, and P. K. Hansma, J. Appl. Phys. **80**, 3622 (1996).
[43]R. Proksch and S. V. Kalinin, Nanotechnology **21**, 455705 (2010).
[44]C. P. Green and J. E. Sader, Phys. Fluids **17**, 073102 (2005).
[45]R. J. Clarke, O. E. Jensen, and J. Billingham, Phys. Rev. E **78**, 056310 (2008).
[46]M. J. Higgins, R. Proksch, J. E. Sader, M. Polcik, S. Mc Endoo, J. P. Cleveland, and S. P. Jarvis, Rev. Sci. Instrum. **77**, 013701 (2006).
[47]B. Ohler, Rev. Sci. Instrum. **78**, 063701 (2007).
[48]J. R. Lozano, D. Kiracofe, J. Melcher, R. Garcia, and A. Raman, Nanotechnology **21**, 465502 (2010).
[49]J. Park, S. Nishida, P. Lambert, H. Kawakatsu, and H. Fujita, Lab Chip **11**, 4187 (2011).
[50]Doppler shift of the laser reflected from the cantilever causes beating in the interferometer signal, the frequency of which is directly proportional to the cantilever velocity; no additional calibration is necessary.
[51]L. D. Landau and E. M. Lifshitz, *Theory of Elasticity*, 2nd ed. (Pergamon, Oxford, NY, 1970).
[52]Power spectral density data were derived from the time series measurements using MATLAB code, Mathworks, Natick, MA.
[53]J. E. Sader, B. D. Hughes, J. A. Sanelli, and E. J. Bieske, Rev. Sci. Instrum. **83**, 055106 (2012).
[54]SI reference data for viscosity and density were obtained from the National Institute of Standards and Technology; see http://webbook.nist.gov/chemistry/name-ser.html
[55]J. E. Sader, J. Sanelli, B. D. Hughes, J. P. Monty, and E. J. Bieske, Rev. Sci. Instrum. **82**, 095104 (2011).
[56]W. E. Newell, Science **161**, 1320 (1968).
[57]F. R. Blom, S. Bouwstra, M. Elwenspoek, and J. H. J. Fluitman, J. Vac. Sci. Technol. B **10**, 19 (1992).
[58]R. Sandberg, A. Boisen, and W. Svendsen, Rev. Sci. Instrum. **76**, 125101 (2005).